Article

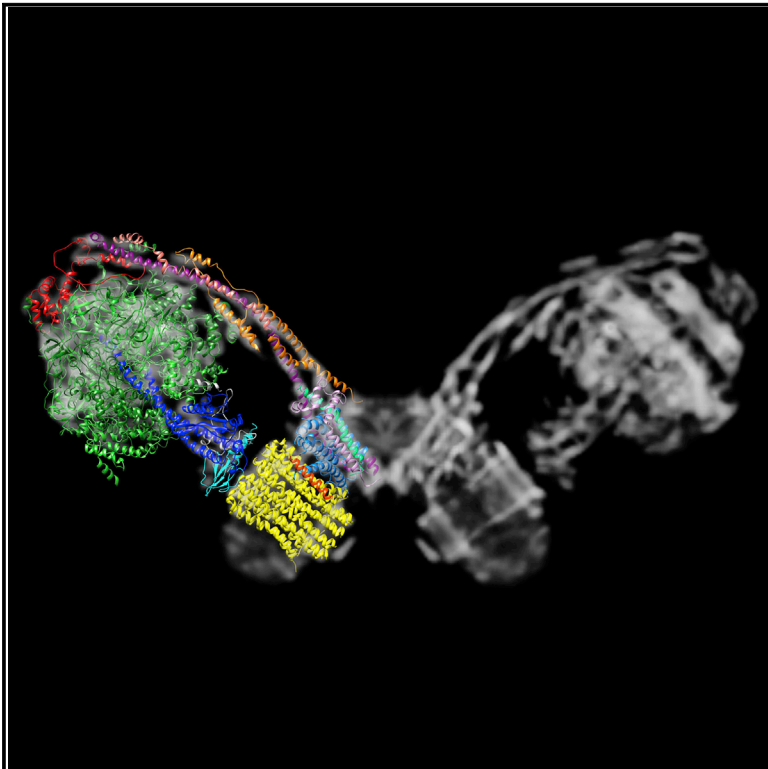# Structure of a Complete ATP Synthase Dimer Reveals the Molecular Basis of Inner Mitochondrial Membrane Morphology

Graphical Abstract

Highlights

- Cryo-EM structure of a yeast F_1F_o-ATP synthase dimer

- Inhibitor-free X-ray structure of the F_1 head and rotor complex

- Mechanism of ATP generation by rotary catalysis

- Structural basis of cristae formation in the inner mitochondrial membrane

Authors

Alexander Hahn, Kristian Parey, Maike Bublitz, ..., Janet Vonck, Werner Kühlbrandt, Thomas Meier

Correspondence

werner.kuehlbrandt@biophys.mpg.de (W.K.), t.meier@imperial.ac.uk (T.M.)

In Brief

ATP synthases are complex macromolecular machines that supply most of the ATP in cells. Hahn et al. present the structure of a complete ATP synthase dimer, which provides insights into both the mechanism of these nanomotors and how they cause membrane bending to form cristae in the inner mitochondrial membrane.

Accession Numbers

5FL7

CrossMark

CellPress

Structure of a Complete ATP Synthase Dimer Reveals the Molecular Basis of Inner Mitochondrial Membrane Morphology

Alexander Hahn,[1] Kristian Parey,[1] Maike Bublitz,[2,4] Deryck J. Mills,[1] Volker Zickermann,[3] Janet Vonck,[1] Werner Kühlbrandt,[1,*] and Thomas Meier[1,5,*]

[1]Department of Structural Biology, Max Planck Institute of Biophysics, Max-von-Laue-Str. 3, 60438 Frankfurt am Main, Germany
[2]Institute of Biochemistry
[3]Institute of Biochemistry II, Medical School
Goethe University Frankfurt, Max-von-Laue-Str. 9, 60438 Frankfurt am Main, Germany
[4]Present address: Department of Biochemistry, University of Oxford, South Parks Road, Oxford OX1 3QU, UK
[5]Present address: Department of Life Sciences, Imperial College London, Exhibition Road, London SW7 2AZ, UK
*Correspondence: werner.kuehlbrandt@biophys.mpg.de (W.K.), t.meier@imperial.ac.uk (T.M.)
http://dx.doi.org/10.1016/j.molcel.2016.05.037

SUMMARY

We determined the structure of a complete, dimeric F_1F_o-ATP synthase from yeast *Yarrowia lipolytica* mitochondria by a combination of cryo-EM and X-ray crystallography. The final structure resolves 58 of the 60 dimer subunits. Horizontal helices of subunit *a* in F_o wrap around the *c*-ring rotor, and a total of six vertical helices assigned to subunits *a, b, f, i,* and *8* span the membrane. Subunit *8* (*A6L* in human) is an evolutionary derivative of the bacterial *b* subunit. On the lumenal membrane surface, subunit *f* establishes direct contact between the two monomers. Comparison with a cryo-EM map of the F_1F_o monomer identifies subunits *e* and *g* at the lateral dimer interface. They do not form dimer contacts but enable dimer formation by inducing a strong membrane curvature of ~100°. Our structure explains the structural basis of cristae formation in mitochondria, a landmark signature of eukaryotic cell morphology.

INTRODUCTION

The mitochondrial F_1F_o-ATP synthase produces most of the ATP in the cell by rotary catalysis and plays a crucial role in severe human neurodegenerative disorders (Kucharczyk et al., 2009). The proton motive force (pmf) across the inner membrane drives the *c*-ring rotor in the membrane-embedded F_o subcomplex, generating the torque that powers a sequence of conformational changes in the membrane-extrinsic F_1 subcomplex, resulting in ATP generation (Abrahams et al., 1994; Boyer, 1997; Noji et al., 1997). The F_o subcomplex is connected to F_1 by the central stalk, which transmits torque to the catalytic head, and the peripheral stalk, which acts as a stator to prevent idle rotation of the F_1 head with the *c*-ring.

Dimers of the ATP synthase shape the inner mitochondrial membrane and mediate cristae formation (Davies et al.,

2012; Paumard et al., 2002). The ATP synthase forms rows of V-shaped dimers along the highly curved edges of inner membrane cristae (Strauss et al., 2008). The dimer angle is 86° in yeasts and metazoans, but different in mitochondria of plants (Davies et al., 2011) and algae (Allegretti et al., 2015). Recently, the complete structure of the dimeric mitochondrial ATP synthase of the chlorophyll-less green alga *Polytomella* sp. was reported at 6.2 Å resolution, revealing the unexpected feature of a horizontal four-helix bundle in the *a* subunit of the F_o subcomplex (Allegretti et al., 2015). The long horizontal helices are conserved not only in mammalian mitochondria (Zhou et al., 2015) and bacteria (Morales-Rios et al., 2015) but also in the more distantly related V-type and A-type ATPases (Zhao et al., 2015), and are thus a fundamental feature common to all rotary ATPases (Kühlbrandt and Davies, 2016). Together with the *c*-ring rotor, the horizontal helices of subunit *a* create two aqueous half-channels on either side of the membrane (Allegretti et al., 2015; Kühlbrandt and Davies, 2016). The *c* subunits in the rotor ring bind and release protons as the ring rotates through the alternating hydrophobic environment of the lipid bilayer and the aqueous environment of the half-channels (Allegretti et al., 2015; Meier et al., 2011, 2005; Pogoryelov et al., 2010; Symersky et al., 2012), thereby generating the torque for ATP synthesis.

The recently reported structures include the dimeric form of an ATP synthase that has unusual peripheral stalks (Allegretti et al., 2015), and the monomer of the bovine complex (Zhou et al., 2015) as well as a bacterial ATP synthase (Morales-Rios et al., 2015), which both appear to be incomplete. There is currently no structure of an ATP synthase dimer that closely resembles the mammalian complex. Mitochondrial ATP synthases from yeasts have a subunit composition very similar to the mammalian (human) ATP synthase and form the same V-shaped dimers. By a combination of cryoelectron microscopy (cryo-EM) and X-ray crystallography, we have obtained the structure of the complete ATP synthase dimer from the aerobic, genetically accessible yeast *Yarrowia lipolytica*, in which ATP synthase dimers were previously reported (Davies et al., 2011; Nübel et al., 2009). The combined maps resolve 58 of the 60 known

Table 1. Table of Crystallography

	Y. lipolytica F_1c_{10}
Data Collection	
Wavelength (Å)	1.008
Space group	$P2_12_12$
Cell dimensions: a, b, c (Å)	169.5, 182.2, 193.0
Cell dimensions: α, β, γ (°)	90, 90, 90
Resolution (Å)	49.19–3.50 (3.60–3.50)[a]
Total reflections	1,477,286 (119,821)[a]
Unique reflections	75,882 (6,046)[a]
R_{merged}	18.2 (>100)[a]
$I / \sigma(I)$	9.84 (0.61)[a]
Completeness (%)	99.99 (100.0)[a]
Redundancy	19.5 (19.8)[a]
Refinement	
Resolution (Å)	3.50
R_{work} / R_{free} (%)	27.39 / 30.54
Wilson β factor	158
Average β factor (Å²)	167
No. atoms	30,123
Protein	29,954
Ligands	152
Water	17[b]
RMSDs: bond lengths (Å)	0.006
RMSDs: bond angles (°)	0.883
PDB code	5FL7

[a]Values in parentheses are for highest-resolution shell.
[b]Water molecules coordinated to Mg^{2+} in the nucleotide binding sites (Figure S2E).

protein subunits and the inhibitor protein *IF1*. The structure reveals the previously unknown subunit architecture of the dimer interface in the membrane, thereby providing major new insights into mitochondrial membrane architecture.

RESULTS

Isolation and Biochemistry of *Yarrowia lipolytica* ATP Synthase Dimers

ATP synthase dimers from *Y. lipolytica* were purified from dodecylmaltoside (DDM)-solubilized mitochondrial membranes by centrifugation in a digitonin-containing glycerol gradient, followed by anion exchange chromatography. Two-dimensional gel electrophoresis and liquid chromatography-mass spectrometry (LC-MS) indicated that the $2YLF_1F_o$ (*Y. lipolytica* ATP synthase dimer) fraction contained all ATP synthase subunits, including *e*, *g*, and *k*, which are known as dimer specific (Arnold et al., 1998) (Figure S1; Table S1, available online). The DDM-purified monomeric *Y. lipolytica* ATP synthase ($1YLF_1F_o$) lacks subunits *e*, *g*, and *k*. The ATP hydrolysis activity of both $1YLF_1F_o$ and $2YLF_1F_o$ is ∼2.25 U/mg. F_o is coupled to 95% and 75%, respectively, as determined by oligomycin inhibition. The lower percentage of coupled complexes in $2YLF_1F_o$ is most likely due to free F_1 subcomplexes and detergent in the dimer preparation

(Figure S1A). The similarly high activities of $2YLF_1F_o$ and $1YLF_1F_o$ indicate that the two ATP synthase monomers within the dimer operate independently in ATP hydrolysis mode.

F_1c_{10} Crystal Structure

Crystals of the YLF_1c_{10} subcomplex were obtained from the $1YLF_1F_o$ complex. Whereas previous crystallographic studies of similar complexes (Giraud et al., 2012; Pagadala et al., 2011; Stock et al., 1999) used an excess of nucleotide substrates or inhibitors to trap functional states, we crystallized YLF_1c_{10} without any such additives to ensure similar conditions for crystallography and cryo-EM. The 3.5 Å X-ray structure of YLF_1c_{10} (Table 1; Figures S2A–S2D) reveals that all three non-catalytic α subunits bind Mg·ATP in their nucleotide sites. Of the three catalytic β subunits, one is empty (β_E), while both the β_{DP} and β_{TP} sites (Abrahams et al., 1994) contain Mg·ADP (Figures 1 and S2E).

Cryo-EM Structure of the *Yarrowia lipolytica* ATP Synthase Dimer

We determined the structure of the $2YLF_1F_o$ by single-particle cryo-EM (Figure 2A). After 2D and 3D classification, 38,679 particles were selected for reconstruction of a 3D map with C2 symmetry imposed. The central stalks of the two monomers include an angle of ∼100°. Masking one monomer in the dimer during 3D refinement improved the resolution to 6.9 Å for the F_1 subcomplex and masking the F_o dimer improved it to 6.2 Å, as determined by gold-standard Fourier shell correlation (Figure S4). The long helices in the peripheral stalks and the F_o part of the stator are the best-resolved features (Movie S1). The resolution of the F_1c_{10} subcomplex in the cryo-EM map is slightly lower, due to minor variations in the dimer angle (Figures S3D and S3E) and to differences in rotational position of the rotor assembly. Further classification revealed that the position of the central stalk varies independently in both monomers (Figures S3F and S3G), confirming that the two ATP synthase assemblies in the dimer function independently, as already suggested by the similar ATPase hydrolysis activities of $1YLF_1F_o$ and $2YLF_1F_o$.

Classification of the same dataset with one monomer in the dimer masked enabled us to distinguish three different rotational states of the F_1 head assembly, with two out of three positions favored, in which the positions of the central stalk differ by ∼120° or 240° (Figures S3H and S3I). Interaction with the central stalk affects the nucleotide binding domains and C-terminal domains of the β subunits (Figure S3I). The three conformations show the three "Boyer states," open, loose, and tight (Boyer, 1997), of the *Y. lipolytica* complex as seen in the YLF_1c_{10} crystal structure (Movies S2 and S3), similar to the crystal structure of the bovine F_1 complex (Abrahams et al., 1994). The three states are trapped in energy wells, which stall the rotor in defined positions upon dissipation of the pmf by the membrane-solubilizing detergent.

In the most populated class (45% of the particles; subclass 2 in Figures S3H and S3I), a rod-like density protrudes from the $\alpha_{DP}\beta_{DP}$ pair close to the peripheral stalk (Figure 2D). This density superposes precisely on the inhibitor *IF1* in an X-ray structure of the bovine mitochondrial F_1F_o-ATP synthase with *IF1* bound (Gledhill et al., 2007). The presence of *IF1* in ATP synthases prepared from large-scale yeast fermentations is not unexpected,
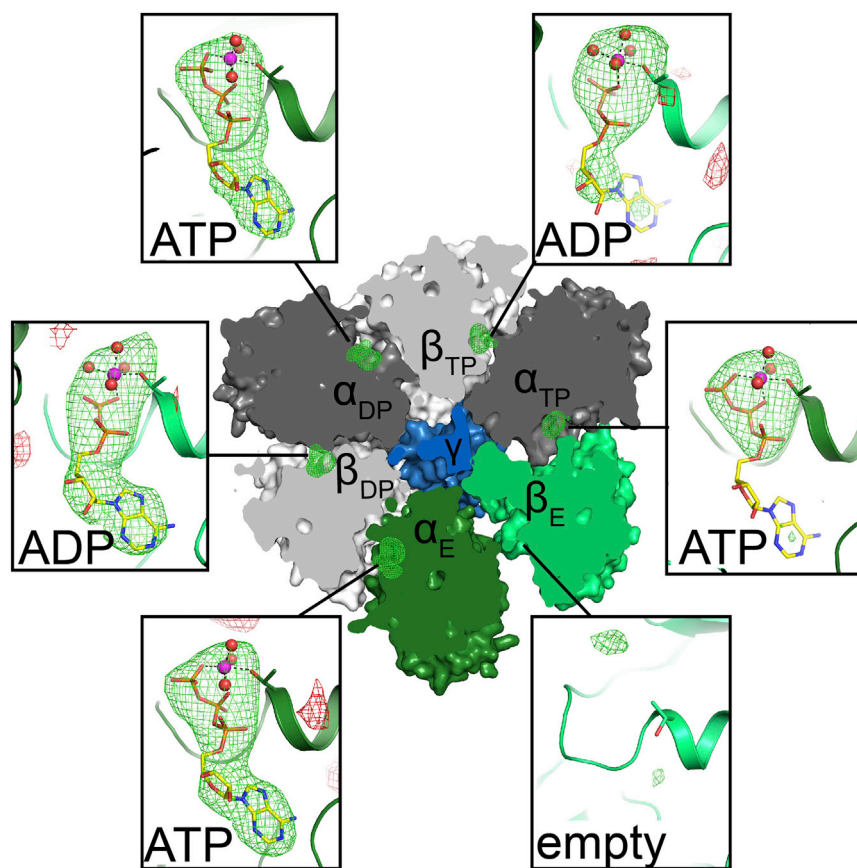
Figure 1. Nucleotide Binding Sites in *Yarrowia lipolytica* F$_1$c$_{10}$

Cross section through the F$_1$ X-ray structure shows the six nucleotide binding sites at the α/β subunit interfaces viewed from the matrix. Subunits α (dark green, dark gray) and β (light green, light gray) are arranged around the central γ subunit (blue). Green and red mesh indicates unbiased mF_{obs}-DF_{calc} nucleotide difference densities contoured at 3.0σ and −3.0σ, respectively. Boxed, close-up views of Walker A nucleotide binding motifs (cartoon) with αThr202, βThr195, and nucleotides in stick representation. Mg^{2+} ions with coordinated water molecules are shown as spheres. Atoms of C, N, O, P, and Mg are colored yellow, blue, red, orange, and magenta, respectively. Positive difference densities match Mg·ATP [·3 H$_2$O] in all three α sites, and Mg·ADP[·4 H$_2$O] in β$_{DP}$ and β$_{TP}$. The β$_E$ site is empty. The conformational flexibility of the β$_E$ subunit is a possible cause of the weaker adenosine density of the ATP in the adjacent α$_{TP}$ site. See Figure S3 for further difference maps after modeling various nucleotides in the α and β sites.

as oxygen concentration of these cultures can decrease, which reduces the matrix pH and triggers *IF1* binding, as observed with yeast grown on non-fermentable substrates (Satre et al., 1975). The fact that *IF1* is found in only one of the three classes is, however, surprising.

Peripheral Stalk

The peripheral stalk consists of several long, well-resolved α helices, which were traced without ambiguity (Figures 2A–2C). Homology models based on crystal structures of the bovine subunits *b*, *d*, and *OSCP* (Dickson et al., 2006; Rees et al., 2009) were fitted to the soluble sector of the *Y. lipolytica* peripheral stalk, which has the same subunit composition (Table S1). Subunit *h* has only 20% sequence identity to the equivalent bovine *F6* (Fujikawa et al., 2015), accounting for the observed structural differences. The overall curvature of the peripheral stalk differs from that in the bovine crystal structure, but resembles that in the cryo-EM map of the monomeric bovine complex (Baker et al., 2012), suggesting that crystal contacts affect stalk curvature. As in the bovine complex (Zhou et al., 2015), helices 1 and 5 of *OSCP* on the F$_1$ head are in contact with the N terminus of α$_E$ (Rees et al., 2009). Two further close contacts are found at the N terminus of α$_{TP}$, which interacts with helices 4 and 5 of *OSCP*, and at the N terminus of α$_{DP}$, which intercalates between the peripheral stalk helices. The N terminus of this α subunit forms a previously unrecognized four-helix bundle with *b*, *h*, and the C terminus of *OSCP*, which positions the F$_1$ head and bonds it to the peripheral stalk (Figure 2B). The contacts in this interaction are mainly hydrophobic, except for those mediated by the conserved residues αGlu33 and αArg41. The *d* subunit interacts with the C terminus of the α$_{DP}$ subunit, displacing it toward the peripheral stalk by 5 Å relative to the *YLF$_1$c$_{10}$* X-ray structure (Figure 2C). Below the F$_1$ head, peripheral stalk subunits *d* and *b* bend toward the central stalk. The density of subunit *b*, which is thought to have two trans-membrane helices at its N terminus (Figure S4), continues without interruption into the membrane.

Helix Assignment in the F$_o$ Stator

The *Y. lipolytica* F$_o$ stator subcomplex comprises the eight membrane protein subunits *a*, *b*, *e*, *f*, *g*, *i*, *k*, and *8*. The F$_o$ part of each monomer contains ten well-defined α-helical densities enveloped by a detergent micelle that features the characteristic ∼90° dimer membrane curvature (Davies et al., 2012) (Figure 2A). Six of these densities indicate trans-membrane α helices, numbered 1–6 in Figures 3A and 3B and assigned in Figure 3C. The loops connecting the helices are, for the most part, not visible at this resolution, but the helix segments can be identified on the basis of sequence comparison, secondary structure predictions, proximity, and known helix topology.

Subunit b

Helix 1 is the continuation of the peripheral stalk subunit *b* and is thus the second trans-membrane helix of *b*. Helix 2 is close to it and is the most likely candidate for the first trans-membrane helix of this subunit. The second-nearest helix 3 is too far for the short, six-residue loop connecting the two trans-membrane helices of subunit *b* (Figure S4A).

Subunit a

Sequence alignment of subunit *a* indicates a consistent pattern of seven characteristic consecutive protein regions (Figure S5A):
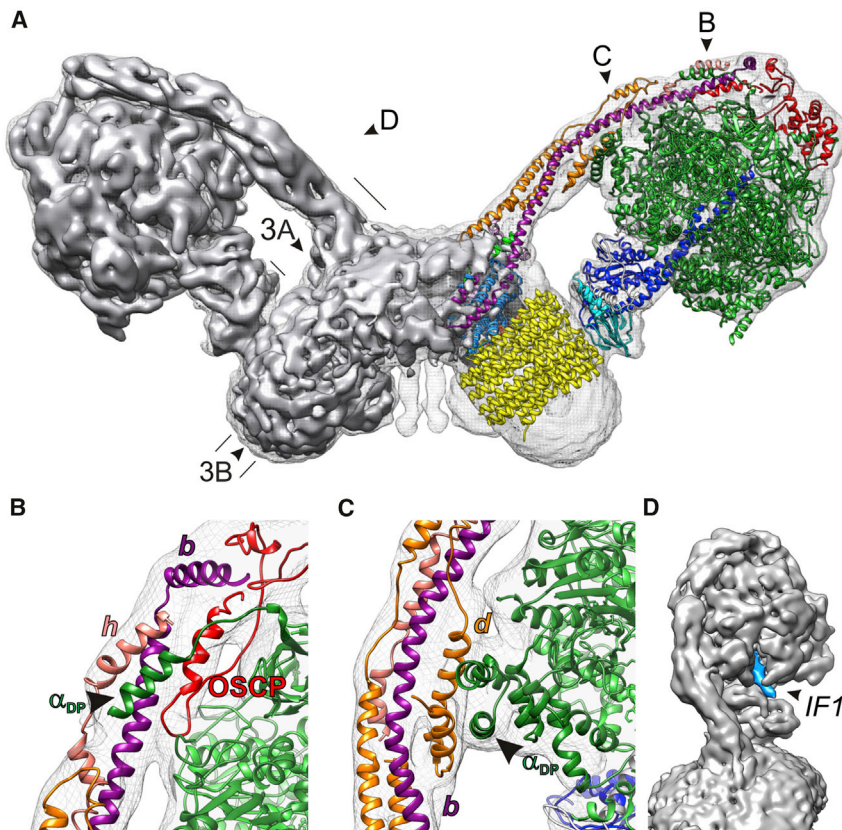
Figure 2. Cryo-EM Structure of the *Yarrowia lipolytica* F₁Fₒ-ATP Synthase Dimer

(A) Side view of the map (gray surface and volume). The monomer on the right was fitted in Coot (Emsley et al., 2010) with the X-ray structure of the *Y. lipolytica* F_1c_{10} complex and homology models of peripheral stalk subunits based on atomic models from the *B. taurus* outer stalk structures (PDB: 2WSS and 2CLY) (Figures 1 and S2E). Cross sections shown in Figures 3A and 3B and viewing directions for (B)–(D) are indicated.

(B and C) Detailed views of peripheral stalk subunit interactions as indicated in (A). (B) Upper and (C) lower section. Dark and light green, α and β subunits, respectively; light blue, subunit a; yellow, c_{10} ring; blue, subunit γ; cyan, subunit δ; light gray, subunit ε; purple, subunit *b*; orange, subunit *d*; salmon, subunit *h*; red, OSCP.

(D) The intrinsic inhibitor protein *IF1* (light blue) binds in the α/β$_{DP}$ site proximal to the peripheral stalk. The overall map resolution of 7.8 Å in (A) improved upon masking to 6.9 Å for the F₁ complex (B–D). Movie S1 is a video of the rotating complete ATP synthase dimer.

glutamate (Cain, 2000; Eya et al., 1991; Lightowlers et al., 1987). Our assignment places this residue and a series of conserved charged or polar residues in the long horizontal hairpin at the subunit *a/c* interface (see Discussion). Our *a* subunit assignment is fully consistent with that of the bovine (Zhou et al., 2015) and *Paracoccus* ATP synthase (Morales-Rios et al., 2015), but the order of helices *a*H5 and *a*H6 with respect to the *Polytomella* assignment (Allegretti et al., 2015) is reversed.

Subunit 8

Helix 4 (green in Figure 3) has a short matrix extension with a slight kink toward the *c*-ring. We assign this density to the small, 48-residue subunit *8* (Figure S4B). Subunit *8* has a conserved N-terminal MPQL motif located in the intermembrane space (IMS) (Stephens et al., 2000), followed by a trans-membrane helix, terminated in yeasts by the conserved Pro33, and a short hydrophilic C-terminal stretch. This sequence fits the density well, with Pro33 at the kink. The trans-membrane helix of subunit *8* has a short connecting density in the IMS toward the *c*-ring and below the first helix hairpin of the *a* subunit, which accommodates the conserved MPQL motif. Thus, the N terminus of subunit *8* appears to anchor the horizontal four-helix bundle of subunit *a* in its position within the Fₒ assembly.

The longer mammalian subunit *8* has been shown to interact at its C terminus with the peripheral stalk subunits *b* and *d* (Lee et al., 2015); in plant mitochondria, subunit *8* is as long as a typical *b* subunit. This subunit was thought to have no prokaryotic equivalent (Lee et al., 2015; Stephens et al., 2003), but comparison with the *b* subunit of α-proteobacteria, which share a common ancestor with mitochondria, strikingly reveals the same N-terminal MPQL motif. Therefore, the mitochondrial subunit *8* derives from one of the two *b* subunits of its bacterial
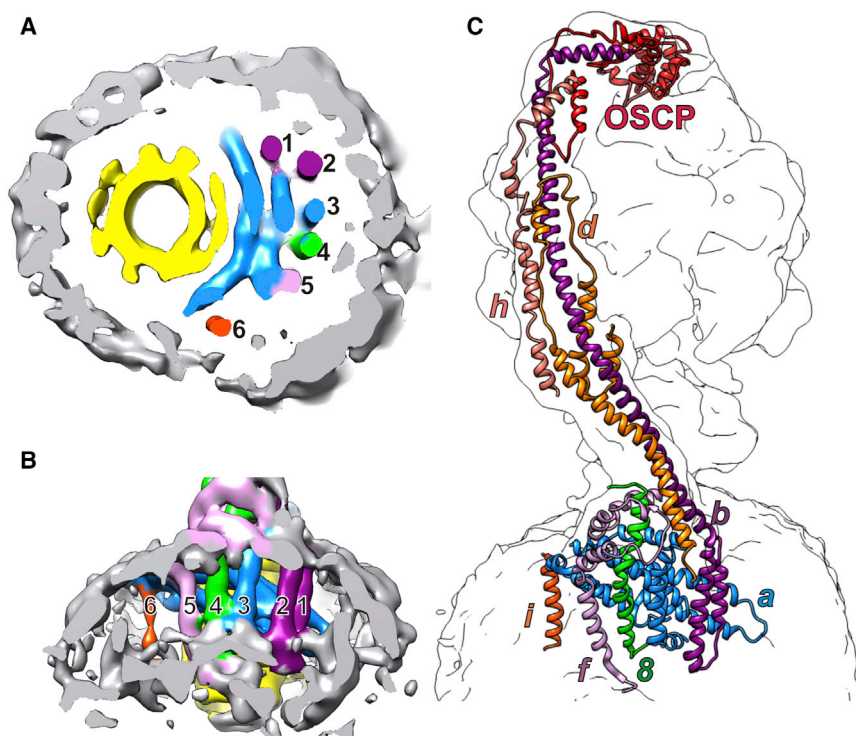
(i) the hydrophilic N terminus; (ii) a ~20 residue hydrophobic stretch indicative of a trans-membrane helix; (iii) a region rich in hydrophilic and polar residues, prone to form an amphipathic helix (Figure S5B); (iv) two hydrophobic sequences separated by charged or polar side chains; (v) a region with several positively charged residues followed by (vi) a proline-rich region; and finally (vii) an extensive hydrophobic stretch with interspersed, highly conserved charged and polar residues.

We can assign region (iii), the amphipathic helix *a*H2, to the straight helix density on the matrix side just above the horizontal four-helix bundle (Figure 4). Region (ii), the trans-membrane helix of subunit *a*, which we refer to as *a*H1, would thus be helix density 3 in the map (Figures 3 and 4). The N-terminal region (i) of subunit *a* is small, is without clear predicted secondary structure, and has no discernible map density. Regions (iv) to (vii) are assigned to the two membrane-intrinsic helix hairpins of subunit *a* (which we refer to as *a*H3 to *a*H6) on the basis of their striking similarity to the same feature in the *Polytomella* dimer map (Allegretti et al., 2015). The assignment of the two shorter helices as *a*H3 and *a*H4 follows from their proximity to the amphipathic helix *a*H2 (Figure 4). The non-helical regions (v) and (vi) link the two helix hairpins, but only limited density is visible for them in the map. We assign the longest helix in the four-helix bundle, which follows the curve of the *c*-ring closely, to *a*H5 in the first half of region (vii), and the second helix in this hairpin to helix *a*H6 in the C-terminal half of this region (Figure 4). Helix *a*H5 contains the essential Arg182, which interacts with the protonatable *c*-ring

Figure 3. Assignment of the *Yarrowia lipolytica* F$_1$F$_o$-ATP Synthase Stator Region

(A and B) Cross sections through the F$_o$ stator region as indicated in Figure 2A. (A) View from the matrix and (B) from the membrane. Four horizontal and six vertical helix densities (labeled 1–6) next to the c_{10} ring rotor (yellow) in the detergent micelle (gray) were assigned to stator subunits. Blue, subunit *a*; purple, subunit *b*; green, subunit *8*; lavender, subunit *f*; dark orange, subunit *i*.

(C) Overview of peripheral stalk and stator subunits in the cryo-EM map. The overall map resolution of 7.8 Å in Figure 2A improved upon masking to 6.2 Å for the F$_o$ dimer (A and B) and 6.9 Å for the F$_1$ complex (C).

ancestor and is truncated in the mammalian and fungal lines. Subunit *8* is one of the few mitochondrially encoded ATP synthase components in *Y. lipolytica*, together with the *a* and *c* subunits (Kerscher et al., 2001), consistent with its bacterial origin.

Subunit *f*

Helix 5 (lavender in Figure 3) is the most likely candidate for the nuclear-encoded trans-membrane subunit *f*. In yeast, this 100-residue subunit has a hydrophilic N-terminal domain on the matrix side and a predicted C-terminal trans-membrane helix (Figure S4C). Three curved densities at the base of the peripheral stalk (Figure 3B) that surround the matrix extension of subunit *8* are assigned to the N terminus of subunit *f*. The sharp changes in direction between the densities assigned to this subunit are consistent with the positions of conserved prolines in the *f* subunit sequence alignment.

Subunit *i*

Finally, the density of helix 6 (orange in Figures 3A and 3B) is weaker than the others. Based on its position next to the *a* subunit, we assign it to the yeast-specific, non-essential subunit *i*, which is present in both the monomer and the dimer in *Y. lipolytica* (Table S1) and has been shown to interact with subunits *a*, *f*, *d*, and *g* (Paumard et al., 2000).

Our assignments are fully consistent with all previously reported chemical crosslinking results of ATP synthases from yeasts, metazoans, and bacteria (DeLeon-Rangel et al., 2013; Jiang and Fillingame, 1998; Schwem and Fillingame, 2006; Stephens et al., 2003) (Figure S6).

Subunits *e* and *g* at the Dimer Interface

We collected a cryo-EM dataset of 1*YL*F$_1$F$_o$ and generated a 3D map of the monomeric *Y. lipolytica* ATP synthase at 8.4 Å resolution (Figure 5). Unlike the dimer, 1*YL*F$_1$F$_o$ does not contain the

dimer-specific subunits *e*, *g*, and *k* (Table S1). The bovine monomer has subunits *e* and *g*, but not *k* (Baker et al., 2012). A comparison of the 3D map volumes therefore reveals the location of *e* and *g* in the dimer map (Figures 5D and 5F). They occupy a roughly triangular density on the dimer interface next to the N-terminal trans-membrane helices of subunit *b*, with a narrow extension that protrudes ∼40 Å into the IMS. This density is similar to the *e/g* density assigned in the bovine monomer (Zhou et al., 2015), but the orientation of the IMS extension is different (see below).

Subunit *e* is predicted to have an N-terminal trans-membrane helix with a conserved, essential GxxxG motif, a signature of helix-helix interaction (Arselin et al., 2003), and a hydrophilic C terminus that would account for the IMS extension. The *g* subunit can be crosslinked to the N terminus of *b* in the matrix (Soubannier et al., 1999). Deleting the first trans-membrane helix of *b* results in the loss of *g* and dissociation of the dimer (Soubannier et al., 2002), indicating that *g* contributes to dimer stability.

Subunit *g* consists of an N-terminal matrix domain and a predicted C-terminal trans-membrane helix that likewise contains a conserved GxxxG motif. Subunits *e* and *g* may thus form a tight heterodimer in the membrane via their GxxxG motifs. The helices in such a tight heterodimer would not be resolved at 6.2 Å, like the inner helices of the *c*-ring, which are known to interact through such motifs (Vonck et al., 2002). There is no contact between the *e/g* density of one monomer to any subunit of the other, so *e* and *g* do not participate directly in dimer formation. Side views of the bovine and *Y. lipolytica* maps (Figure S7A) indicate that each *e/g* heterodimer bends the membrane by ∼50°, resulting in the ∼100° kink observed in the dimer. The most prominent direct dimer contact is formed by the C-terminal domain of subunit *f* (Figure 6). The C terminus of subunit *f* contains conserved charged and polar residues that would mediate this interaction (Figure S3C). The membrane curvature induced by subunits *e* and *g* appears to be necessary to position the C-terminal domains of the *f* subunits in both monomers for interaction across the interface, resulting in dimer formation.
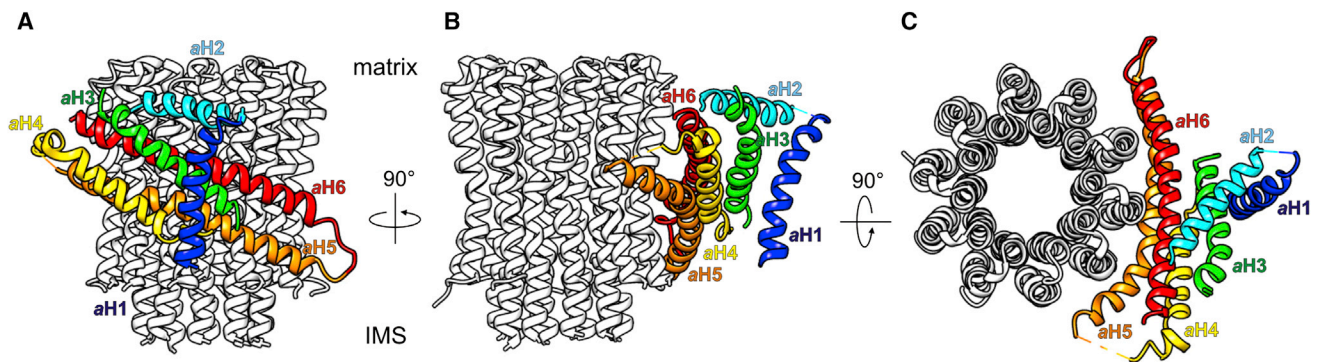
Figure 4. Subunit *a*

View (A) from the dimer interface, (B) along the *a/c* interface, and (C) from the matrix. The hydrophilic N terminus on the IMS side (region (i) in the text) is not resolved. Helix *a*H1 (blue, region (ii)) is the only vertical trans-membrane helix of subunit *a*. The amphipathic helix *a*H2 (cyan, region (iii)) runs along the matrix membrane surface. The membrane-intrinsic helices *a*H3 (green) and *a*H4 (yellow) of region (iv) form a hairpin. Regions (v) and (vi) are the unresolved connection between helices *a*H4 and *a*H5. The membrane-intrinsic helices *a*H5 (orange) and *a*H6 (red) form a second, longer hairpin (region (vii)), tilted by 20°–25° relative to the membrane plane. *a*H5 follows the curve of the *c*-ring (light gray) closely. *a*H5 and *a*H6 are ∼70 Å long and in contact with 3–4 *c* subunits, while the helices in the distal hairpin, *a*H3 and *a*H4, are ∼45 and ∼35 Å long; neither is in direct contact with the *c*-ring. The *a*H4/*a*H5 hairpin loop is on the IMS side, while the C terminus is exposed on the matrix surface. All six *a* subunit helices are highly conserved (Figure S5).

DISCUSSION

Rotational F$_1$ States

A detailed comparison of the *YL*F$_1c_{10}$ crystal structure to the bovine (Abrahams et al., 1994) and *Saccharomyces cerevisiae* (Kabaleeswaran et al., 2006) F$_1$ and F$_1c_{10}$ complexes (Figure S8) reveals that the three conformational states of the corresponding α/β heterodimers are very similar in the two yeast species, with root-mean-square deviation (RMSD) values below 1.7 Å, while nucleotide binding and C-terminal regions of the bovine β subunits differ (Table S2; Movies S4 and S5). In *YL*F$_1c_{10}$ both the β$_E$ and the β$_{DP}$ site are more open than in the bovine complex, while their β$_{TP}$ sites are similar. Overall, the three β subunits resemble one another more closely in *Y. lipolytica* than in the bovine and *S. cerevisiae* complexes (Figure S8B).

Aligning the γ subunits in all F$_1$ X-ray structures and comparing the relative positions of the conserved P loop in the β$_{DP}$ subunit (Figure S8A), we find that the *YL*F$_1c_{10}$ P loop is shifted to a position that, in bovine F$_1$ (Rees et al., 2012), would indicate a post-hydrolysis or pre-product release state. The post-hydrolysis position of the γ subunit in *YL*F$_1c_{10}$ agrees with the presence of bound Mg·ADP in the catalytic β$_{DP}$ and β$_{TP}$ sites. Since *YL*F$_1c_{10}$ was crystallized without added nucleotides, the ADP originates from ATP hydrolysis during isolation or crystallization (Abrahams et al., 1996; Gledhill et al., 2007). The fact that ADP is present in the *Y. lipolytica* β$_{DP}$ at this late stage of hydrolysis without addition of nucleotide-stabilizing azide (Bowler et al., 2006) is surprising, as ADP was not found in the binding sites of other F$_1$ complexes crystallized under similar conditions (Bianchet et al., 1998; Stocker et al., 2007). This might indicate a higher nucleotide affinity of the *Y. lipolytica* β$_{DP}$ site. In contrast, phosphate (P$_i$) was not detected in the β$_{DP}$ and β$_{TP}$ sites, in line with a possible alternative leaving route for P$_i$, as described for *S. cerevisiae* F$_1$ (Kabaleeswaran et al., 2006).

We found the inhibitor protein *IF1* bound to one of the three different rotational F$_1$ states in the cryo-EM maps, but not in the *YL*F$_1c_{10}$ X-ray structure, indicating that it was lost during crystallization. By contrast, *IF1* was present in all seven rotary states in the cryo-EM maps of monomeric bovine F$_1$F$_o$-ATP synthase (Zhou et al., 2015), as would be expected since the complex was purified by *IF1* affinity chromatography. Apart from the absence of *IF1* in the β$_{DP}$ region (Figure 2D), the 3.5 Å *YL*F$_1c_{10}$ crystal structure matches the dimer map closely (Figures 2A, S3H, and S3I). Like the X-ray structure, the cryo-EM map therefore shows a post-hydrolysis state.

Structure of the F$_o$ Stator

The subunit *a* structure is remarkably conserved in F$_1$F$_o$-ATP synthases. Densities for all six helices of our *Y. lipolytica* structure are also present in the same orientations in the cryo-EM map of the bovine heart monomer (Zhou et al., 2015), while four helices are present in the recent 4 Å X-ray structure of the bacterial complex (Morales-Rios et al., 2015) (Figure S7B). The *Polytomella* cryo-EM map (Allegretti et al., 2015) has elements that correspond to each of the six *a* subunit helices in *Y. lipolytica*, even though the polypeptide sequences diverge. The other *Polytomella* stator subunits do not resemble those of yeasts, metazoans, or bacteria.

The cryo-EM map of the bovine monomer shows four trans-membrane helices, two of which were identified as belonging to the peripheral stalk subunit *b*, and one each to subunits *a* and *A6L* (subunit 8 in fungi) (Zhou et al., 2015). All helices superpose well on our map and the assignment agrees with ours, except that there is no density for the *f* subunit in the bovine map (Zhou et al., 2015). Although the bovine complex prepared according to Runswick et al. (Runswick et al., 2013) should contain the *f* subunit, this subunit was not identified by Zhou et al. Subunit *f* may have dissociated during isolation of the bovine monomer, suggesting that it is not firmly attached. As the *f* subunit is responsible for direct dimer contacts in our assignment (Figure 6), its dissociation from the bovine complex
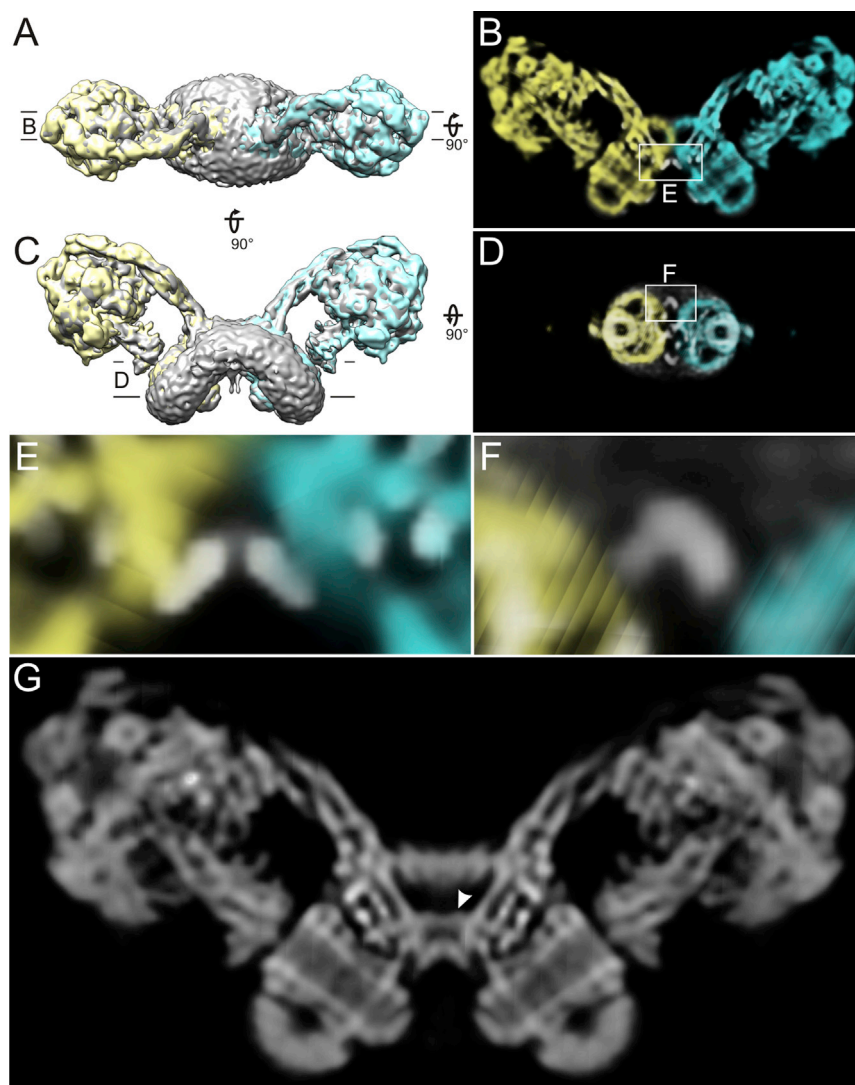
A

B

C

D

E

F

G

Figure 5. Dimer Interface

(A) Matrix view of the *Y. lipolytica* ATP synthase cryo-EM dimer map (gray) with superposed monomer maps (yellow and blue).

(B) Vertical slice through monomer maps as indicated in (A). Dimer contacts are mediated by protein densities outside the detergent micelle of the monomer (boxed).

(C) Side view of superposed maps in (A).

(D) Horizontal slice through the dimer interface as indicated in (C). The white density (boxed) belongs to membrane subunits present in the dimer, but not in the monomer. LC-MS analysis of monomer and dimer subunit composition identifies these subunits as *e* and *g* (Table S1).

(E) Detailed view of the lumenal dimer contacts as indicated in (B).

(F) Detailed view of the density assigned to the dimer-specific subunits *e* and *g* as indicated in (D).

(G) Central slice of the dimer. A sheet-like density (arrowhead) connecting subunits *a* and *8* may be the yeast-specific subunit *k*, the only unassigned protein in the dimer map.

may explain why dimers from mammalian mitochondria are, in our experience, less stable.

The X-ray structure of the bacterial F_1F_o complex from *Paracoccus denitrificans* (Morales-Rios et al., 2015) shows only two of the trans-membrane helices in the F_o stator, which superpose well on the trans-membrane helix of subunit *8* and *a*H1 in the *Y. lipolytica* dimer (panel (iv) in Figure S7B). Therefore, these helix densities, which were unassigned in the *Paracoccus* map, belong to one of the two bacterial *b* subunits and the trans-membrane helix of subunit *a* (*a*H1), lending strong support to our conclusion that mitochondrial subunit *8* derives from a bacterial *b* subunit. Surprisingly, the trans-membrane helix of the second *b* subunit seems to be completely absent in the *Paracoccus* structure, indicating that it is flexible or disordered in the 4 Å X-ray map.

Proton Translocation through F_o

Ion translocation through F_o is mediated by the *a* subunit and the *c*-ring (Figure 7). A number of high-resolution X-ray structures of

ATPase *c*- or *K*-rings have shown that the conserved glutamate residues in the *c* subunits lock the protons (or Na^+) in the hydrophobic environment of the lipid bilayer (Meier et al., 2005; Murata et al., 2005; Pogoryelov et al., 2009) but open to release the ions in a hydrophilic environment (Mizutani et al., 2011; Pogoryelov et al., 2010; Symersky et al., 2012). The recent cryo-EM structures of the *Polytomella* ATP synthase and *S. cerevisiae* V-type ATPase indicate two aqueous half-channels at the subunit *a/c* interface that are thought to conduct protons to and from the *c*-ring protonation sites (Allegretti et al., 2015). We find similar aqueous half-channels in equivalent positions of the *Y. lipolytica* dimer map (Figures 7A and 7B). Conserved hydrophilic residues of *a*H5 and *a*H6 line the aqueous cavity on the matrix side (Figures 7C and 7D). The conserved charged and polar residues of *a*H5, starting with Glu168 four helix turns upstream of Arg182, create the hydrophilic environment to release the proton from the opposing *c* subunit glutamate into the matrix. The ~20° tilt of the *a*H5/*a*H6 hairpin places the hairpin loop close to the IMS surface, and the C terminus of *a*H6 on the matrix side (Figure 7A). Consequently, the lumenal half-channel near the hairpin loop and the matrix half-channel at the C terminus of subunit *a* are laterally offset, as anticipated (Junge et al., 1997; Vik and Antonio, 1994). The proton entrance channel on the IMS side is likely to include the conserved Asn186 in *a*H5, Asn106 in *a*H3, and the exchangeable pair His191/Glu229 in *a*H5 and *a*H6, one of which is Glu or Asp in all ATP synthases (Figure S5). Rather than mediating proton release, the essential Arg182 would allow only deprotonated *c* subunit glutamate side chains to pass (Figure 7D). Removal of this arginine by mutagenesis uncouples ion
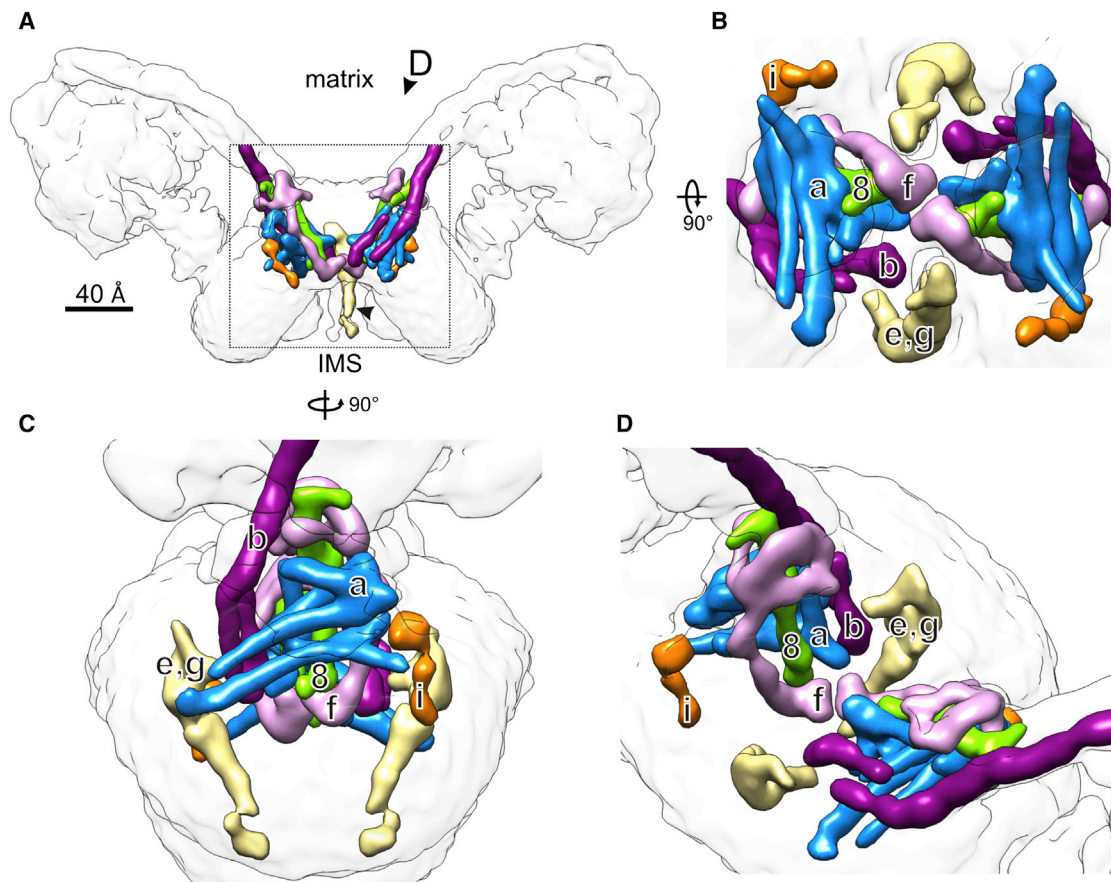
Figure 6. The F$_o$ Stator

Membrane protein densities in the two F$_o$ stator complexes of the *Y. lipolytica* ATP synthase dimer. Subunits *a*, *b*, *f*, *i*, and *8* are colored as in Figure 2. Subunits *e* and *g* are ivory.

(A) Side view of the dimer interface. The IMS extensions of subunit *e* (arrowhead) were segmented at a lower contour level. F$_o$ subunits of the two ATP synthase monomers interact on the IMS side. A 40 Å gap on the matrix side contains lipid or detergent.

(B) View from the IMS. The C-terminal segment of subunit *f* mediates a direct protein contact between the two monomers in the dimer. Densities on either side of the protein contact are assigned to subunits *e* and *g* (see Figure 6).

(C) View from the *c*-ring.

(D) Oblique view in the direction indicated in (A). For an evaluation of Cys-Cys crosslinks, see Figure S6 and Table S3.

translocation from ATP synthesis (Mitome et al., 2010), as it results in futile proton translocation without *c*-ring rotation.

Clinical studies show that mutations in *a*H5 and *a*H6 impair the functionality or assembly of ATP synthase in human mitochondria (Kucharczyk et al., 2009; Xu et al., 2015), giving rise to severe neuropathological disorders (Houstek et al., 2006), such as the maternally inherited Leigh syndrome or retinitis pigmentosa (Kucharczyk et al., 2009). A molecular understanding of the exact ion translocation mechanism is essential for exploring future therapy. The structure of the genetically accessible *Y. lipolytica* ATP synthase now provides a basis for structural and functional studies to combat these diseases at the molecular level.

Dimer Contacts

In the *Y. lipolytica* F$_1$F$_o$ dimer, which contains subunits *e* and *g*, the detergent belt is bent by roughly 100°. In the bovine F$_1$F$_o$ monomer, which contains subunits *e* and *g*, it is bent by ~50° (Baker et al., 2012; Zhou et al., 2015), but in the *Y. lipolytica*

monomer, which lacks *e* and *g*, the belt is more or less straight (Figure S7A; Table S1). We conclude that *e* and *g* are chiefly responsible for inducing the membrane curvature that results in mitochondrial cristae morphology.

There is no evident function for the C-terminal IMS helix of subunit *e* in the dimeric complex (Figure 6A). In contrast to the bovine map (Zhou et al., 2015), this elongated density protrudes straight out of the F$_o$ stator region into the IMS, while in the bovine map it is curved and contacts the central plug of the *c*-ring. A role in the formation of higher-order ATP synthase oligomers and dimer rows (Strauss et al., 2008; Davies et al., 2012) seems unlikely, as the extension is not easily accessible and appears to point in the wrong direction for interaction between adjacent dimers (Figure 5D). Moreover, the dimer spacing along the rows is irregular (Daum et al., 2013), which suggests that the inter-dimer protein contacts are dynamic. Instead, the subunit *e* extension with its predicted coiled-coil propensity may play a role in complex assembly.
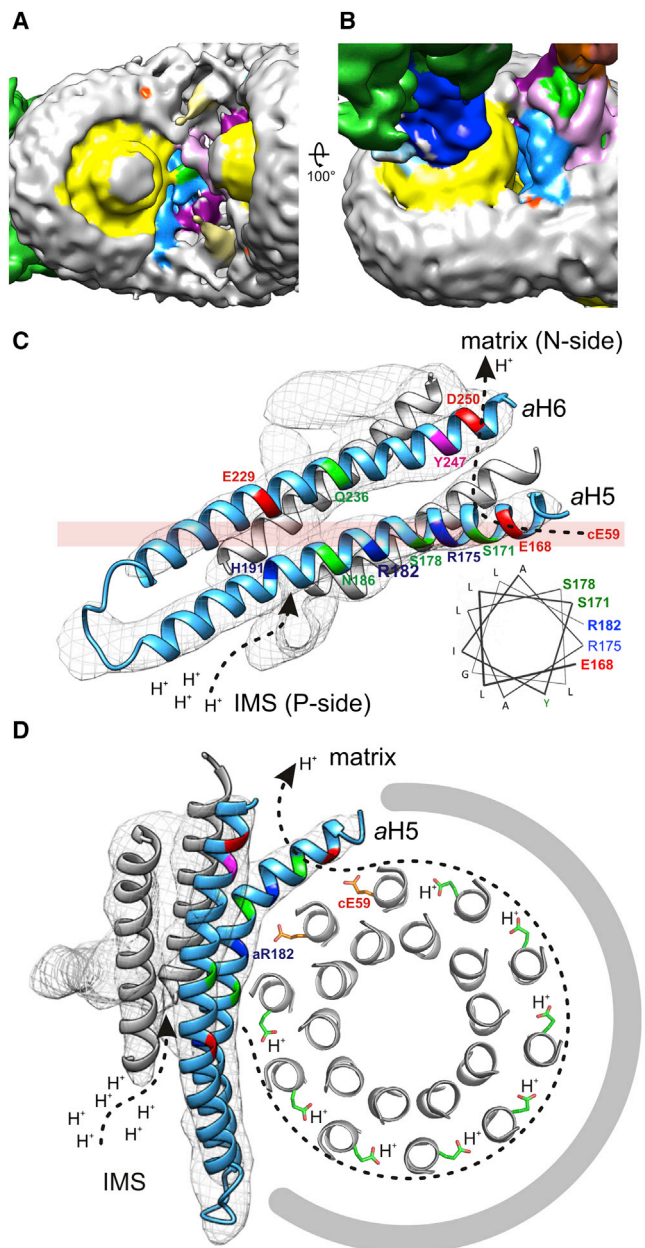
Figure 7. Ion Translocation through F$_o$

(A) IMS surface of the *Y. lipolytica* dimer. Subunits are color coded as in Figure 2. The *c*-ring and the dimer contact region are solvent exposed. *a*H5 of subunit *a* (light blue) is visible from the IMS side. The central plug on the *c*-rings consists of lipid or detergent (Meier et al., 2001).

(B) Oblique view from the matrix shows the gap between the *c*-ring (yellow) and subunit *a* (light blue).

(C) Fitted *a*H5 and *a*H6 hairpin of subunit *a* next to the *c*-ring rotor with modeled positions of conserved positive (blue), negative (red), and polar residues (green). The helical wheel projection (inset) indicates alternating polar, charged, and hydrophobic residues at the start of *a*H5, with polar or charged residues oriented toward the *c*-ring. The transparent pink bar indicates the level at which the protonated *c*-ring glutamates rotate past the strictly conserved *a*Arg182.

(D) Section through the c_{10}-ring (gray) and subunit *a* (gray mesh) with a cartoon model (blue) of the *c*-ring at the level of protonated glutamates in the

The two F$_o$ subcomplexes in the membrane are separated by a wedge-shaped gap that is ~40 Å wide on the matrix side and narrows to ~15 Å on the IMS side (Figures 5G and 6A). On the matrix side, this wedge appears to be filled by lipid or detergent, as there is no distinct protein density. The tip of the wedge on the IMS side contains the dimer contact domain assigned to the C terminus of subunit *f* (Figure 6). The center of the wedge-shaped gap is bridged by a conspicuous sheet of density connecting the trans-membrane helices of subunits *a* and *8* (Figure 5G), which may contribute to dimer formation. It is tempting to speculate that this density belongs to the so far unassigned yeast-specific subunit *k*, a small, partly hydrophilic protein without predicted trans-membrane helix (Figure S4D). The sheet may form a barrier between the membrane leaflet on the matrix side and hydrophilic protein domains on the IMS side of the dimer interface. The matrix half of the wedge-shaped space has the thickness of one membrane leaflet, implying a new and unusual membrane architecture in this region of the dimer.

Role of ATP Synthase Dimers in Membrane Morphology

The comparatively simple bacterial and chloroplast ATP synthases consist of eight or nine different subunits, which are sufficient for ATP production. The chloroplast ATP synthase has been shown to be monomeric (Daum et al., 2010), and no ATP synthase dimers have been reported in bacteria. By contrast, all known mitochondrial ATP synthases form dimers in the membrane that self-assemble into rows (Davies et al., 2012). Mitochondrial ATP synthases of yeasts and metazoans have eight additional subunits of so far unexplained structure and function. Our map shows how the mitochondria-specific subunits in the mitochondrial F$_o$ subcomplex are arranged, and that most of them have a role in dimer formation: the N-terminal trans-membrane extension of *b* anchors *e* and *g* to the complex, and the *e/g* heterodimer induces local membrane curvature, which in turn appears to enable the IMS domain of *f* (and possibly subunit *k*) to establish protein-protein contacts across the dimer interface.

ATP synthase dimer rows are a prerequisite for the formation of inner membrane cristae (Davies et al., 2012), a hallmark signature of mitochondrial morphology. Cristae formation extends the membrane surface to accommodate a large number of respiratory chain complexes, making it possible to meet the high energy demands of eukaryotic cells (Lane and Martin, 2010). They also form a mitochondrial sub-compartment that supports a locally increased proton concentration in the confined cristae space. The structure of the mitochondrial ATP synthase dimer thus offers new insights into how mitochondria became the efficient power plants of eukaryotic cells.

EXPERIMENTAL PROCEDURES

ATP synthase dimers fully competent for oligomycin-sensitive ATP hydrolysis were isolated from mitochondria prepared from large-scale *Yarrowia lipolytica*

---

locked (green) or open (orange) conformation (Pogoryelov et al., 2010; Symersky et al., 2012). *a*H6 peels away from the *c*-ring, accounting for the observed gap at the *a/c* interface. Dashed arrows in (C) and (D) indicate the proton pathway from the IMS (P side) to the matrix (N side), as proposed for the *Polytomella* ATP synthase (Allegretti et al., 2015).

cultures (Kashani-Poor et al., 2001) and purified by glycerol gradient centrifugation, anion exchange, and gel filtration chromatography. Cryo-EM grids of $2YLF_1F_o$ dimers and $1YLF_1F_o$ monomers were prepared and images were recorded on an in-column energy-filtered JEOL 3200 FSC electron microscope with a Gatan K2 direct electron detector in movie mode. Global beam-induced motion was corrected by movie frame processing (Li et al., 2013). Two- and three-dimensional classification and 3D map refinement were carried out with RELION 1.3 (Scheres, 2012). Crystals of the F_1c_{10} subcomplex were grown from concentrated samples of the $1YLF_1F_o$. X-ray data were collected at beamline PX-II X10SA (Swiss Light Source), and the structure was determined by molecular replacement with a model based on the *S. cerevisiae* F_1c_{10} complex (PDB: 2XOK) (Stock et al., 1999).

ACCESSION NUMBERS

The structure coordinates have been deposited in the Protein Data Bank under ID code PDB: 5FL7. The EM data were deposited in the worldwide PDB under ID codes wwPDB: EMD-8151 (symmetric dimer map); EMD-8152 (masked F_o map); and EMD-8153, EMD-8154, and EMD-8155 (subclass 1, 2, and 3 of the masked F_1F_o monomer).

SUPPLEMENTAL INFORMATION

Supplemental Information includes Supplemental Experimental Procedures, eight figures, three tables, and five movies and can be found with this article online at http://dx.doi.org/10.1016/j.molcel.2016.05.037.

AUTHOR CONTRIBUTIONS

T.M. initiated the study; T.M. and W.K. directed the project; V.Z. provided mitochondrial membranes; A.H. purified the protein; D.J.M. devised the cryo-EM data collection procedure; A.H. and D.J.M. collected cryo-EM data; A.H. and J.V. analyzed cryo-EM data; K.P. grew crystals and collected X-ray data; K.P., M.B., and T.M. analyzed X-ray data; T.M., J.V., W.K., K.P., M.B., and A.H. wrote the paper.

ACKNOWLEDGMENTS

REFERENCES

Abrahams, J.P., Leslie, A.G.W., Lutter, R., and Walker, J.E. (1994). Structure at 2.8 Å resolution of F_1-ATPase from bovine heart mitochondria. Nature *370*, 621–628.

Abrahams, J.P., Buchanan, S.K., Van Raaij, M.J., Fearnley, I.M., Leslie, A.G.W., and Walker, J.E. (1996). The structure of bovine F_1-ATPase complexed with the peptide antibiotic efrapeptin. Proc. Natl. Acad. Sci. USA *93*, 9420–9424.

Allegretti, M., Klusch, N., Mills, D.J., Vonck, J., Kühlbrandt, W., and Davies, K.M. (2015). Horizontal membrane-intrinsic α-helices in the stator a subunit of an F-type ATP synthase. Nature *521*, 237–240.

Arnold, I., Pfeiffer, K., Neupert, W., Stuart, R.A., and Schägger, H. (1998). Yeast mitochondrial F_1F_0-ATP synthase exists as a dimer: identification of three dimer-specific subunits. EMBO J. *17*, 7170–7178.

Arselin, G., Giraud, M.F., Dautant, A., Vaillier, J., Brèthes, D., Coulary-Salin, B., Schaeffer, J., and Velours, J. (2003). The GxxxG motif of the transmembrane domain of subunit e is involved in the dimerization/oligomerization of the yeast ATP synthase complex in the mitochondrial membrane. Eur. J. Biochem. *270*, 1875–1884.

Baker, L.A., Watt, I.N., Runswick, M.J., Walker, J.E., and Rubinstein, J.L. (2012). Arrangement of subunits in intact mammalian mitochondrial ATP synthase determined by cryo-EM. Proc. Natl. Acad. Sci. USA *109*, 11675–11680.

Bianchet, M.A., Hullihen, J., Pedersen, P.L., and Amzel, L.M. (1998). The 2.8-Å structure of rat liver F_1-ATPase: configuration of a critical intermediate in ATP synthesis/hydrolysis. Proc. Natl. Acad. Sci. USA *95*, 11065–11070.

Bowler, M.W., Montgomery, M.G., Leslie, A.G.W., and Walker, J.E. (2006). How azide inhibits ATP hydrolysis by the F-ATPases. Proc. Natl. Acad. Sci. USA *103*, 8646–8649.

Boyer, P.D. (1997). The ATP synthase—a splendid molecular machine. Annu. Rev. Biochem. *66*, 717–749.

Cain, B.D. (2000). Mutagenic analysis of the F_0 stator subunits. J. Bioenerg. Biomembr. *32*, 365–371.

Daum, B., Nicastro, D., Austin, J., 2nd, McIntosh, J.R., and Kühlbrandt, W. (2010). Arrangement of photosystem II and ATP synthase in chloroplast membranes of spinach and pea. Plant Cell *22*, 1299–1312.

Daum, B., Walter, A., Horst, A., Osiewacz, H.D., and Kühlbrandt, W. (2013). Age-dependent dissociation of ATP synthase dimers and loss of inner-membrane cristae in mitochondria. Proc. Natl. Acad. Sci. USA *110*, 15301–15306.

Davies, K.M., Strauss, M., Daum, B., Kief, J.H., Osiewacz, H.D., Rycovska, A., Zickermann, V., and Kühlbrandt, W. (2011). Macromolecular organization of ATP synthase and complex I in whole mitochondria. Proc. Natl. Acad. Sci. USA *108*, 14121–14126.

Davies, K.M., Anselmi, C., Wittig, I., Faraldo-Gómez, J.D., and Kühlbrandt, W. (2012). Structure of the yeast F_1F_o-ATP synthase dimer and its role in shaping the mitochondrial cristae. Proc. Natl. Acad. Sci. USA *109*, 13602–13607.

DeLeon-Rangel, J., Ishmukhametov, R.R., Jiang, W., Fillingame, R.H., and Vik, S.B. (2013). Interactions between subunits *a* and *b* in the rotary ATP synthase as determined by cross-linking. FEBS Lett. *587*, 892–897.

Dickson, V.K., Silvester, J.A., Fearnley, I.M., Leslie, A.G.W., and Walker, J.E. (2006). On the structure of the stator of the mitochondrial ATP synthase. EMBO J. *25*, 2911–2918.

Emsley, P., Lohkamp, B., Scott, W.G., and Cowtan, K. (2010). Features and development of Coot. Acta Crystallogr. D Biol. Crystallogr. *66*, 486–501.

Eya, S., Maeda, M., and Futai, M. (1991). Role of the carboxyl terminal region of H^+-ATPase (F_0F_1) a subunit from *Escherichia coli*. Arch. Biochem. Biophys. *284*, 71–77.

Fujikawa, M., Sugawara, K., Tanabe, T., and Yoshida, M. (2015). Assembly of human mitochondrial ATP synthase through two separate intermediates, F_1-*c*-ring and *b*-*e*-*g* complex. FEBS Lett. *589* (19 Pt B), 2707–2712.

Giraud, M.F., Paumard, P., Sanchez, C., Brèthes, D., Velours, J., and Dautant, A. (2012). Rotor architecture in the yeast and bovine F_1-c-ring complexes of F-ATP synthase. J. Struct. Biol. *177*, 490–497.

Gledhill, J.R., Montgomery, M.G., Leslie, A.G.W., and Walker, J.E. (2007). How the regulatory protein, IF1, inhibits F_1-ATPase from bovine mitochondria. Proc. Natl. Acad. Sci. USA *104*, 15671–15676.

Houstek, J., Pícková, A., Vojtísková, A., Mrácek, T., Pecina, P., and Jesina, P. (2006). Mitochondrial diseases and genetic defects of ATP synthase. Biochim. Biophys. Acta *1757*, 1400–1405.

Jiang, W., and Fillingame, R.H. (1998). Interacting helical faces of subunits a and c in the F_1F_0 ATP synthase of *Escherichia coli* defined by disulfide cross-linking. Proc. Natl. Acad. Sci. USA *95*, 6607–6612.

Junge, W., Lill, H., and Engelbrecht, S. (1997). ATP synthase: an electrochemical transducer with rotatory mechanics. Trends Biochem. Sci. *22*, 420–423.

Kabaleeswaran, V., Puri, N., Walker, J.E., Leslie, A.G.W., and Mueller, D.M. (2006). Novel features of the rotary catalytic mechanism revealed in the structure of yeast F_1 ATPase. EMBO J. 25, 5433–5442.

Kashani-Poor, N., Kerscher, S., Zickermann, V., and Brandt, U. (2001). Efficient large scale purification of his-tagged proton translocating NADH:ubiquinone oxidoreductase (complex I) from the strictly aerobic yeast *Yarrowia lipolytica*. Biochim. Biophys. Acta 1504, 363–370.

Kerscher, S., Durstewitz, G., Casaregola, S., Gaillardin, C., and Brandt, U. (2001). The complete mitochondrial genome of *Yarrowia lipolytica*. Comp. Funct. Genomics 2, 80–90.

Kucharczyk, R., Zick, M., Bietenhader, M., Rak, M., Couplan, E., Blondel, M., Caubet, S.D., and di Rago, J.P. (2009). Mitochondrial ATP synthase disorders: molecular mechanisms and the quest for curative therapeutic approaches. Biochim. Biophys. Acta 1793, 186–199.

Kühlbrandt, W., and Davies, K.M. (2016). Rotary ATPases: A new twist to an ancient machine. Trends Biochem. Sci. 41, 106–116.

Lane, N., and Martin, W. (2010). The energetics of genome complexity. Nature 467, 929–934.

Lee, J., Ding, S., Walpole, T.B., Holding, A.N., Montgomery, M.G., Fearnley, I.M., and Walker, J.E. (2015). Organization of subunits in the membrane domain of the bovine F-ATPase revealed by covalent cross-linking. J. Biol. Chem. 290, 13308–13320.

Li, X., Mooney, P., Zheng, S., Booth, C.R., Braunfeld, M.B., Gubbens, S., Agard, D.A., and Cheng, Y. (2013). Electron counting and beam-induced motion correction enable near-atomic-resolution single-particle cryo-EM. Nat. Methods 10, 584–590.

Lightowlers, R.N., Howitt, S.M., Hatch, L., Gibson, F., and Cox, G.B. (1987). The proton pore in the *Escherichia coli* F_0F_1-ATPase: a requirement for arginine at position 210 of the a subunit. Biochim. Biophys. Acta 894, 399–406.

Meier, T., Matthey, U., Henzen, F., Dimroth, P., and Müller, D.J. (2001). The central plug in the reconstituted undecameric c cylinder of a bacterial ATP synthase consists of phospholipids. FEBS Lett. 505, 353–356.

Meier, T., Polzer, P., Diederichs, K., Welte, W., and Dimroth, P. (2005). Structure of the rotor ring of F-type Na^+-ATPase from *Ilyobacter tartaricus*. Science 308, 659–662.

Meier, T., Faraldo-Gómez, J.D., and Börsch, M. (2011). ATP synthase, a paradigmatic molecular machine. In Molecular Machines in Biology, J. Frank, ed. (Cambridge University Press), pp. 208–238.

Mitome, N., Ono, S., Sato, H., Suzuki, T., Sone, N., and Yoshida, M. (2010). Essential arginine residue of the F_0-a subunit in F_0F_1-ATP synthase has a role to prevent the proton shortcut without c-ring rotation in the F_0 proton channel. Biochem. J. 430, 171–177.

Mizutani, K., Yamamoto, M., Suzuki, K., Yamato, I., Kakinuma, Y., Shirouzu, M., Walker, J.E., Yokoyama, S., Iwata, S., and Murata, T. (2011). Structure of the rotor ring modified with N,N'-dicyclohexylcarbodiimide of the Na^+-transporting vacuolar ATPase. Proc. Natl. Acad. Sci. USA 108, 13474–13479.

Morales-Rios, E., Montgomery, M.G., Leslie, A.G.W., and Walker, J.E. (2015). Structure of ATP synthase from *Paracoccus denitrificans* determined by X-ray crystallography at 4.0 Å resolution. Proc. Natl. Acad. Sci. USA 112, 13231–13236.

Murata, T., Yamato, I., Kakinuma, Y., Leslie, A.G.W., and Walker, J.E. (2005). Structure of the rotor of the V-type Na^+-ATPase from *Enterococcus hirae*. Science 308, 654–659.

Noji, H., Yasuda, R., Yoshida, M., and Kinosita, K., Jr. (1997). Direct observation of the rotation of F_1-ATPase. Nature 386, 299–302.

Nübel, E., Wittig, I., Kerscher, S., Brandt, U., and Schägger, H. (2009). Two-dimensional native electrophoretic analysis of respiratory supercomplexes from *Yarrowia lipolytica*. Proteomics 9, 2408–2418.

Pagadala, V., Vistain, L., Symersky, J., and Mueller, D.M. (2011). Characterization of the mitochondrial ATP synthase from yeast *Saccharomyces cerevisae*. J. Bioenerg. Biomembr. 43, 333–347.

Paumard, P., Vaillier, J., Napias, C., Arselin, G., Brèthes, D., Graves, P.V., and Velours, J. (2000). Environmental study of subunit i, a F_0 component of the yeast ATP synthase. Biochemistry 39, 4199–4205.

Paumard, P., Vaillier, J., Coulary, B., Schaeffer, J., Soubannier, V., Mueller, D.M., Brèthes, D., di Rago, J.P., and Velours, J. (2002). The ATP synthase is involved in generating mitochondrial cristae morphology. EMBO J. 21, 221–230.

Pogoryelov, D., Yildiz, O., Faraldo-Gómez, J.D., and Meier, T. (2009). High-resolution structure of the rotor ring of a proton-dependent ATP synthase. Nat. Struct. Mol. Biol. 16, 1068–1073.

Pogoryelov, D., Krah, A., Langer, J.D., Yildiz, Ö., Faraldo-Gómez, J.D., and Meier, T. (2010). Microscopic rotary mechanism of ion translocation in the F_0 complex of ATP synthases. Nat. Chem. Biol. 6, 891–899.

Rees, D.M., Leslie, A.G.W., and Walker, J.E. (2009). The structure of the membrane extrinsic region of bovine ATP synthase. Proc. Natl. Acad. Sci. USA 106, 21597–21601.

Rees, D.M., Montgomery, M.G., Leslie, A.G.W., and Walker, J.E. (2012). Structural evidence of a new catalytic intermediate in the pathway of ATP hydrolysis by F_1-ATPase from bovine heart mitochondria. Proc. Natl. Acad. Sci. USA 109, 11139–11143.

Runswick, M.J., Bason, J.V., Montgomery, M.G., Robinson, G.C., Fearnley, I.M., and Walker, J.E. (2013). The affinity purification and characterization of ATP synthase complexes from mitochondria. Open Biol. 3, 120160.

Satre, M., de Jerphanion, M.B., Huet, J., and Vignais, P.V. (1975). ATPase inhibitor from yeast mitochondria. Purification and properties. Biochim. Biophys. Acta 387, 241–255.

Scheres, S.H. (2012). RELION: implementation of a Bayesian approach to cryo-EM structure determination. J. Struct. Biol. 180, 519–530.

Schwem, B.E., and Fillingame, R.H. (2006). Cross-linking between helices within subunit a of *Escherichia coli* ATP synthase defines the transmembrane packing of a four-helix bundle. J. Biol. Chem. 281, 37861–37867.

Soubannier, V., Rusconi, F., Vaillier, J., Arselin, G., Chaignepain, S., Graves, P.V., Schmitter, J.M., Zhang, J.L., Mueller, D., and Velours, J. (1999). The second stalk of the yeast ATP synthase complex: identification of subunits showing cross-links with known positions of subunit 4 (subunit b). Biochemistry 38, 15017–15024.

Soubannier, V., Vaillier, J., Paumard, P., Coulary, B., Schaeffer, J., and Velours, J. (2002). In the absence of the first membrane-spanning segment of subunit 4 (b), the yeast ATP synthase is functional but does not dimerize or oligomerize. J. Biol. Chem. 277, 10739–10745.

Stephens, A.N., Roucou, X., Artika, I.M., Devenish, R.J., and Nagley, P. (2000). Topology and proximity relationships of yeast mitochondrial ATP synthase subunit 8 determined by unique introduced cysteine residues. Eur. J. Biochem. 267, 6443–6451.

Stephens, A.N., Khan, M.A., Roucou, X., Nagley, P., and Devenish, R.J. (2003). The molecular neighborhood of subunit 8 of yeast mitochondrial F_1F_0-ATP synthase probed by cysteine scanning mutagenesis and chemical modification. J. Biol. Chem. 278, 17867–17875.

Stock, D., Leslie, A.G.W., and Walker, J.E. (1999). Molecular architecture of the rotary motor in ATP synthase. Science 286, 1700–1705.

Stocker, A., Keis, S., Vonck, J., Cook, G.M., and Dimroth, P. (2007). The structural basis for unidirectional rotation of thermoalkaliphilic F_1-ATPase. Structure 15, 904–914.

Strauss, M., Hofhaus, G., Schröder, R.R., and Kühlbrandt, W. (2008). Dimer ribbons of ATP synthase shape the inner mitochondrial membrane. EMBO J. 27, 1154–1160.

Symersky, J., Pagadala, V., Osowski, D., Krah, A., Meier, T., Faraldo-Gómez, J.D., and Mueller, D.M. (2012). Structure of the c_{10} ring of the yeast mitochondrial ATP synthase in the open conformation. Nat. Struct. Mol. Biol. 19, 485–491, S1.

Vik, S.B., and Antonio, B.J. (1994). A mechanism of proton translocation by F_1F_0 ATP synthases suggested by double mutants of the a subunit. J. Biol. Chem. 269, 30364–30369.

Vonck, J., von Nidda, T.K., Meier, T., Matthey, U., Mills, D.J., Kühlbrandt, W., and Dimroth, P. (2002). Molecular architecture of the undecameric rotor of a bacterial Na$^+$-ATP synthase. J. Mol. Biol. *321*, 307–316.

Xu, T., Pagadala, V., and Mueller, D.M. (2015). Understanding structure, function, and mutations in the mitochondrial ATP synthase. Microb. Cell *2*, 105–125.

Zhao, J., Benlekbir, S., and Rubinstein, J.L. (2015). Electron cryomicroscopy observation of rotational states in a eukaryotic V-ATPase. Nature *521*, 241–245.

Zhou, A., Rohou, A., Schep, D.G., Bason, J.V., Montgomery, M.G., Walker, J.E., Grigorieff, N., and Rubinstein, J.L. (2015). Structure and conformational states of the bovine mitochondrial ATP synthase by cryo-EM. eLife *4*, e10180.